View metadata, citation and similar papers at core.ac.uk

brought to you by CORE

provided by Open Archive Toulouse Archive Ouverte

Open Archive Toulouse Archive Ouverte (OATAO)

OATAO is an open access repository that collects the work of Toulouse researchers and makes it freely available over the web where possible

This is an author's version published in: **http://oatao.univ-toulouse.fr/24343**

Official URL: https://doi.org/10.1016/j.matchemphys.2019.122059

To cite this version:

Miquelot, Adeline and Despotopoulou, Myrto and Vahlas, Constantin and Villeneuve-Faure, Christina and Dragoe, Nita and Prud'homme, Nathalie and Debieu, Olivier *Morphological, structural, optical, and electrical study of nanostructured thin films: Charge transport mechanism of p-type Co3O4.* (2020) Materials Chemistry and Physics, 240. 122059. ISSN 0254-0584

Any correspondence concerning this service should be sent
to the repository administrator: tech-oatao@listes-diff.inp-toulouse.fr

Morphological, structural, optical, and electrical study of nanostructured thin films: Charge transport mechanism of p-type Co_3O_4

Adeline Miquelot [a], Myrto Despotopoulou [a], Constantin Vahlas [a], Christina Villeneuve [b], Nita Dragoe [c], Nathalie Prud'homme [c], Olivier Debieu [a,*]

[a] *CIRIMAT, Université de Toulouse, Toulouse, France*
[b] *LAPLACE, Université de Toulouse, Toulouse, France*
[c] *ICMMO, Université Paris Sud, Orsay, France*

HIGHLIGHTS

- Polynanocrystalline Co_3O_4 films were deposited by pulsed injection thermal MOCVD.
- Co_3O_4 are p-type semiconductor with a maximum holes mobility of 0.16 cm^2 V^{-1} s^{-1}.
- P-type semiconductor behavior was demonstrated with a maximum holes mobility of 0.16 cm^2 V^{-1} s^{-1}.
- 3-D variable range hopping conduction mechanism of holes was established.
- The results bring direct proof of electrical conduction path through the grains.

GRAPHICAL ABSTRACT

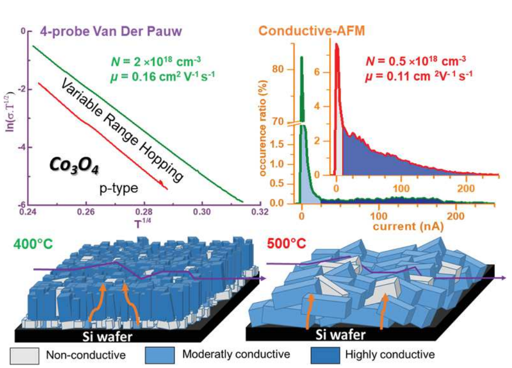

1. Introduction

The normal cubic spinel Co_3O_4 ($Co^{2+}Co_2^{3+}O_4^{2-}$) is the most stable crystalline cobalt oxide and is a promising material for many applications due to its high abundance, low cost, and low toxicity. Co_3O_4 is successfully used as magnetic material [1], as supercapacitor [2,3], as electrochromic windows [4], as well as corrosion protective coatings [5]. It is noteworthy that Co_3O_4 is a direct p-type semiconductor and is extensively studied in photovoltaics cells [6], in gas sensors [7], in anode materials in lithium-ion batteries [8] and in photocatalysis [9]. Low band gap, large surface exchange and high conductivity are essential properties for the achievement of efficient photocatalytic materials. A large variety of physical and chemical deposition methods are available to tailor the films microstructures and their inherent physical and electrochemical properties. In particular, various Co_3O_4 deposition methods have been reported as epitaxy [10,11], magnetron sputtering [12,13], pulsed laser deposition [6], thermal oxidative decomposition method [4], chemical spray pyrolysis [3,14], sol–gel processes like dip coating [15], metal organic chemical vapor deposition (MOCVD) [16], plasma enhanced MOCVD [9], pulsed liquid injection MOCVD [5], and atomic layer deposition (ALD) [17,18]. Moreover, the electrical properties are strongly related to the deposition method. MOCVD [16] and ALD [18,19] dense thin films show the lowest resistivity ranging from 0.5 to 100 Ω cm, while sol-gel [20], chemical

* Corresponding author.

E-mail addresses: adeline.miquelot@ensiacet.fr (A. Miquelot), myrtodesp@gmail.com (M. Despotopoulou), constantin.vahlas@ensiacet.fr (C. Vahlas), christina.villeneuve@laplace.univ-tlse.fr (C. Villeneuve), nathalie.prudhomme@u-psud.fr (N. Dragoe), nita.dragoe@u-psud.fr (N. Prud'homme), olivier.debieu@ensiacet.fr (O. Debieu).

https://doi.org/10.1016/j.matchemphys.2019.122059

precipitation [21], and spray pyrolysis [3,22–24] deposition methods show lower conductive films with resistivity of about two orders of magnitude higher. The main hypothesis to explain this significant difference is the morphology and the grain size. The conduction paths in the highest conductive Co_3O_4 thin films is discussed as grain boundaries [18] or through the grains by variable range hopping (VRH) conduction of holes as proposed by Cheng et al. [16]. However, to the best of our knowledge, the latter hypothesis is not demonstrated experimentally using nano-scale characterization. In this context, the main objective of this paper is to investigate the influence of the Co_3O_4 morphology on the electrical properties at macro and nanoscale.

In the following, we study the effect of two substrate temperatures (Ts) of 400 °C and 500 °C on the morphology, on the optical and the electrical properties of ~140-nm-thick Co_3O_4 films deposited by thermally activated pulsed liquid-gas injection MOCVD.

2. Materials and methods

2.1. Film deposition

Co_3O_4 thin films are deposited on P low-doped (1–20 Ω cm) and As high-doped (0.001–0.005 Ω cm) 300-μm-thick Si (100) wafers, as well as on 1-mm-thick fused silica windows (all Neyco), in a vertical, cylindrical, and stagnant flow cold wall stainless steel MOCVD reactor described elsewhere [25]. The precursor is 99.9% pure tris(2,2,6,6-tetramethyl-3, 5-heptanedionato) cobalt (III) ($Co(dmp)_3$, Strem Chemicals) [26]. It is used as a 0.02 M solution in anhydrous toluene (99.8% Sigma–Aldrich) which is vaporized by pulsed liquid-gas injection using a two-chamber injector (Vapbox 500, Kemstream). Operation of the equipment at 5 Hz and 2.3 m s opening time generates a vapor flow of 0.4 g. min-1, which is transported to the deposition chamber with 200 sccm N_2. An additional gas inlet supplies 200 sccm O_2. Depositions take place at 10 Torr at 400 and 500 °C during 30 and 60 min, respectively, in order to obtain films with constant and homogenous thicknesses of ~140 nm.

2.2. Composition, morphological, crystal and optical characterizations

Films compositions are investigated by electron probe microanalysis (EPMA) using a Cameca SXFive instrument, and by X-ray photoelectron spectroscopy (XPS) using a ThermoScientific K-alpha apparatus. X-ray dispersive spectra are analyzed by Layer Quant add on of PeakSight software. Depth analysis of the composition is probed by XPS after sequential 2 keV Ar^+-etching. Films morphology is characterized by scanning electron microscopy (SEM) using a field emission FE-SEM Jeol JSM-6700 F instrument after Pt-metallization and by atomic force microscopy (AFM) using a Bruker multimode 8 microscope. Samples deposited on Si wafer are analyzed by reflection spectroscopic ellipsometry (SE) with an incidence angle of 70° using a Semilab SE-2000 apparatus. The SE data are analyzed by the Semilab SEA software using a multi-layer architecture composed of a mixture of Co_3O_4 and void using a Bruggeman effective medium approach. With this optical model, the fit regression goodness is over 0.99. SE analysis provides film thickness, effective refractive index, and porosity. The optical absorption spectra of thin films deposited on fused silica windows are measured by transmission and reflection spectroscopy, using an Agilent-Cary 5000 spectrophotometer equipped with an integrating sphere. The crystal structure is investigated by X-ray diffraction (XRD) in a Bruker-D8 diffractometer equipped with a Cu Kα ($\lambda_{K\alpha Cu}$ = 0.154 nm) anode in theta-theta mode with a −3° offset (angular step of 0.03°, and acquisition time of 4 s). Mid-infrared (MIR-FTIR) and far-infrared (FIR-FTIR) Fourier transformed infrared spectra are recorded with a PerkinElmer Frontier, and a Nicolet iS50 Thermo-Fischer Scientific spectrometer, respectively, with 4 and 128 accumulations, respectively, with a common resolution of 4 cm^{-1}. The transmission spectra of thin films deposited on Si wafer are obtained at normal and 60° incidence. The spectra are subsequently corrected from the Si substrate contribution and from optical interferences fringes.

2.3. Electrical characterizations

Macroscale film surface charge transport is probed on films deposited on insulating fused silica windows by a laboratory-made system in a Janis He-free cryostat CCS 200/204 coupled with a Sumitomo SHI-APD 204 cryocooler. The temperature is controlled to within ±50 mK by a Lakeshore 335 controller reading a Si-670 diode thermometer anchored on the cold finger of the cryostat. Measurements are performed on a 4-point probe van der Pauw configuration formed by Pt plots covered by a thin Ag layer. Measurements are made under vacuum ($<10^{-5}$ mbar) by using a Labview home-made program which controls several equipments on GPIB and PXI interfaces. The current is supplied by a Keithley 6220 source for all van der Pauw configurations. The voltage is measured by a Keithley 2182 nanovoltmeter. Several measurements (typically 8) are done for each temperature and the measurement error is thus estimated. Since low carrier mobility samples cannot be reliably measured by standard DC fields [27], room temperature Hall effect measurements are performed in AC-field mode using a 1-T permanent magnet in a Halbach configuration [28]. Measurements are made by applying current with a Keithley 6221 source and by measuring the AC signal with a Zurich Instrument MFLI lock in amplifier. The nanoscale charge transport is locally probed by the atomic force microscope (see section 2.1) in conductive mode (C-AFM) using a PtSi tip in contact (tip radius of 28 nm). A contact force of 100 nN and a sensor sensitivity of 100 nA/V are used. The C-AFM tip collects the current while a positive bias ranging from 1 to 5 V is applied on the high-doped Si substrate.

3. Results and discussion

3.1. Film composition

The films composition is investigated by EPMA. The analysis of the X-ray dispersive spectra are done considering a 140-nm-thick 2-layers film architecture consisting of a thin carbon layer on the surface of the cobalt oxide layer. We found that the surface carbon layers thicknesses are of 2.4 and 1.2 nm, and that the cobalt oxide layers are composed of 42.3 ± 1.2 and 43.1 ± 1.2 at.% of Co, for the 400 °C and 500 °C film, respectively. Co/O ratios are close to the Co_3O_4 stoichiometry (0.73 ± 0.03 and 0.76 ± 0.03 for the 400 °C and 500 °C film, respectively). Nevertheless, lower densities of 4.5 and 4.6 g cm^{-3} for the 400 °C and 500 °C film, respectively, should be used to accurately fit the spectra rather than the bulk density of Co_3O_4 (6.11 g cm^{-3}). The lower densities are explained by the presence of voids created during the film growth that are visible in the FE-SEM images (see Fig. 2) and confirmed by SE analysis (see section 3.2). The evolution of x-ray photoelectron spectra (not shown here) as a function of the Ar^+-etching duration, used to probe the composition as a function of the depth, shows that the carbon-contamination is predominantly located at the surface which is in full agreement with the EPMA analysis. The carbon content may be generated during the deposition and/or during exposition to air. We also observed that the Ar^+-etching considerably reduces the O-content. Then, the effects of the Ar^+-etching on the nature (composition, crystal structure, and morphology) of the oxides prevent any depth analysis of the Co_3O_4 films.

3.2. Structural and morphological characterizations

Fig. 1 shows the XRD pattern of the films deposited on Si wafer. The XRD peaks can all be unambiguously attributed to the spinel Co_3O_4 crystallographic structure. One can notice that the 400°C-X-ray diffractogram is significantly closer to the reference powder pattern than the 500°C-one. This comparison suggests that the nanocrystallites of the 400°C-film are more randomly oriented than in the more textured 500 °C-one.

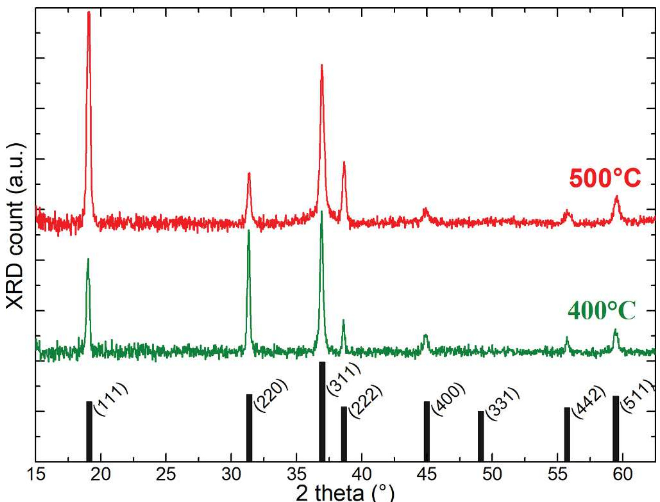

Fig. 1. XRD of Co_3O_4 thin films deposited on Si wafer at 500 °C and 400 °C. The JCPD pattern of Co_3O_4 powder (01-071-2120) is shown for comparison.

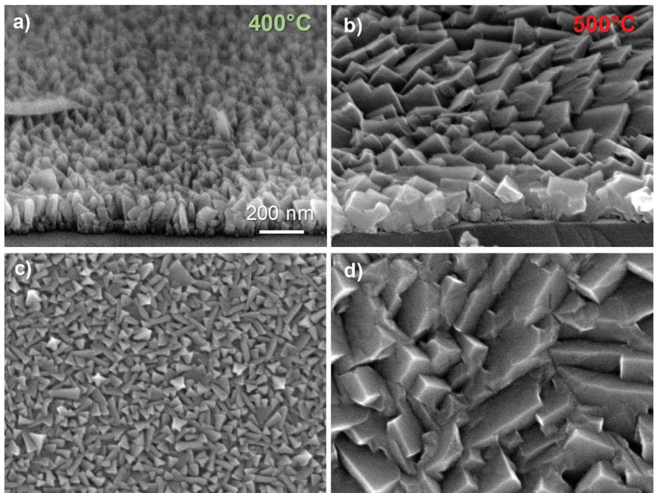

Fig. 2. a), b) 25°-tilted and c), d) top view FE-SEM images of Co_3O_4 films deposited on Si wafer at 400 °C and 500 °C, respectively.

Fig. 2 shows the FE-SEM images of the ~140-nm-thick Co_3O_4 films deposited at 400 °C and 500 °C on Si wafer. The 500 °C film (see Fig. 2b, d) is composed of compact parallelepiped structures of lateral sizes ranging from 150 to 300 nm. This morphology results in a surface roughness of about 50 nm. In contrast, the 400°C-film (see Fig. 2a,c) shows significantly smaller nanostructures and can be considered as a 3-layer architecture. It is composed of a first layer of compact ~40-nm high grains at the Si wafer surface, of a second layer composed of columnar structures forming an upper rough 40-nm-thick third layer at the surface. Fig. 3a shows the measured Co_3O_4 SE angles of the thin films deposited on Si wafer at 500 °C, as well as the simulated SE angles following the multi-layers architectures (Fig. 3b) which are established according to the SEM observations (*i.e.* 3 layers for the 400°C-film and 2 layers for the 500°C-film). The total thicknesses are of 145 and 130 nm for the films deposited at 400 °C and 500 °C, respectively. The architecture of the 500°C-film consists of a dense (2.8% vol. Fraction of void) Co_3O_4 layer and of a 30-nm highly porous roughness layer, which is in agreement with the FE-SEM observations, while the porosity of the 3-layers architecture of the 400°C-film significantly increases from the Si substrate to the surface. This may reflect the depth evolution from the substrate to the surface of the porosity generated by the nanostructures.

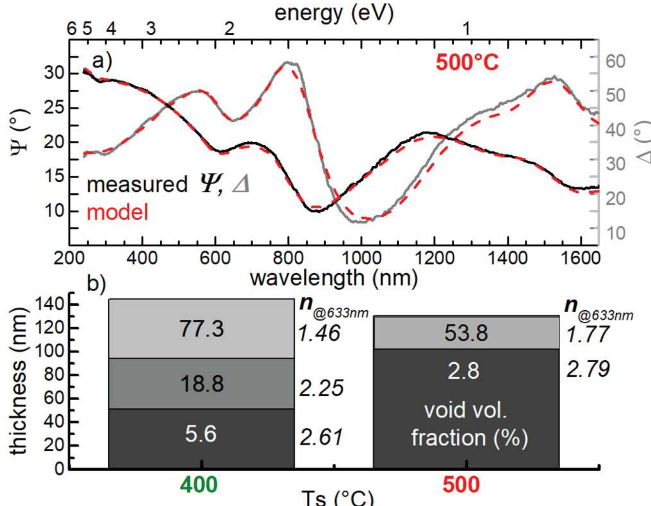

Fig. 3. a) SE angles of Co_3O_4 thin films deposited on Si wafer at 500 °C compared with a model following b) the multilayer architectures at Ts = 400 °C and 500 °C. The volume fraction of void and the effective refractive index at 633 nm of the layers are reported.

Subsequently, this evolution results in an increase of the effective refractive index from the surface to the substrate (see Fig. 3b) which appears to be less abrupt in the 400 °C-film than in the 500 °C sample.

3.3. Optical properties

Fig. 4 a shows the UV–vis–NIR total reflectance spectra. One can see that the total reflection spectra of the 400°C-film is significantly lower than the 500°C-one. This can be explained by the less abrupt graded refractive index architecture of the 400°C-film as revealed by SE analysis (see Fig. 3b). The reflection is mainly specular in the vis-NIR spectral domain. Nevertheless, in the UV region, it is worth noting that only the 500 °C film shows an increase of the diffuse reflected light with decreasing the wavelength. This can be explain by Mie scattering of light from nanostructures sizes larger than ~200 nm which are only observed in FE-SEM in the 500°C-film. Fig. 4b shows the absorption coefficient, α, calculated from the transmission, T, following the expression $\alpha = -log_{10}(T)/t$, where t is the film thickness. The spectra show six optical

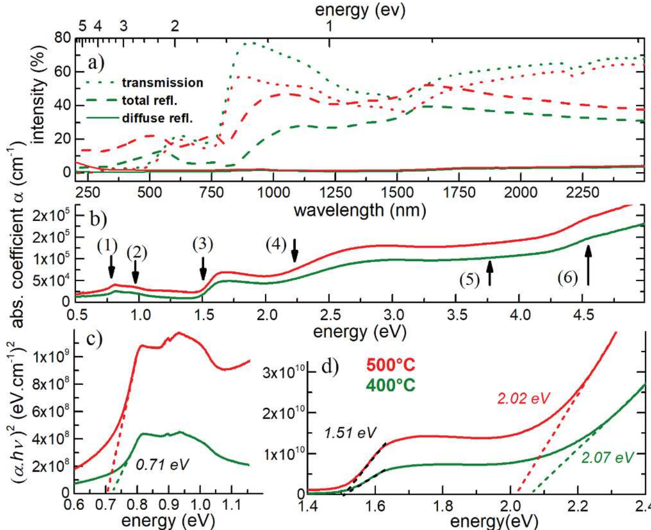

Fig. 4. a) Transmission, total and diffuse reflection spectra of thin films deposited on fused silica windows at 400 °C and 500 °C. b) Absorption coefficient α of the two films. Direct Tauc plot of the c) (1) and d) (3, 4) transitions.

transitions with labeled arrows in agreement with several literature results that identify optical transitions by comparison of the experimental spectra with calculations [10–12]. The direct transition (1) at 0.71 eV is sometimes considered as the Co_3O_4 bandgap originating from a direct forbidden 3d–d transition between tetrahedral-site Co^{2+} cations [11]. Nevertheless, it has also been described as ligand field excitation in the Co_3O_4 structure [12] or due to the presence of polaron or defect states [29]. The 0.9 eV-band (2) is assigned to a metal-to-metal charge transfer reaction between $Co^{2+} \rightarrow Co^{3+}$ cations [11,12] and is discussed as representing an internal oxidation–reduction process [21]. The (3) transition at 1.51 eV is direct and is sometimes considered as the intrinsic Co_3O_4 bandgap [12,29]. It corresponds to a $Co^{3+} \rightarrow Co^{2+}$ transition. The direct (4) transition at 2.02 and 2.07 eV of the 400°C- and of the 500°C-film respectively, is sometimes considered as the effective band by several authors [16,30] who consider the (3) energy level to an acceptor energy level over the edge of the valence band. The (4), (5), and (6) absorption bands corresponds to ligand-to-metal-charge-transfer pathways: $O^- \rightarrow Co^{2+}$, $O^- \rightarrow Co^{3+}$, and $O^{2-} \rightarrow Co^{2+}$ energy levels transitions, respectively. We estimate the (1), (3), and (4) optical absorption thresholds by the interception lines on the x axes of the Tauc plots for direct semiconductors shown in Fig. 4c and d. The values are very close to the ones reported in the literature [11,12] and are particularly in good accordance with the results of Kormondy et al. [10]. This good agreement entirely justifies the use of the Co_3O_4 dielectric function published by the latter authors for the SE simulations.

Fig. 5a shows the normalized FIR-FTIR spectra of the Co_3O_4 thin films deposited on Si wafer. The spectra are recorded with an oblique incidence of 60° that makes longitudinal phonons modes active in addition to transverse ones. We observed four transverse optical modes $TO_{1\text{-}4}$ and two longitudinal modes $LO_{3,4}$ associated to the $TO_{3,4}$ modes. The labels of the $TO_{1,2}$, $TO_{3,4}$, and $LO_{3,4}$ bands are reported in Fig. 5a,b, and c, respectively, as well as their positions which are very close to literature results for Co_3O_4 [13,14]. As Fig. 5a shows, the signal to noise ratio with the FIR-FTIR apparatus is rather low in the low frequencies domain of the $TO_{1,2}$ bands, therefore in the following we focus the analysis on the other vibration modes using a more sensitive apparatus in the MIR. Fig. 5b shows the MIR-FTIR spectra normalized by the film thickness recorded in normal incidence where only the $TO_{3,4}$ absorption bands are active. No noticeable Ts-dependent evolution of their position and linewidth is observed. However, one can notice that the 500°C-bands are slightly more intense than the 400 °C ones that is due the higher density of the 500°C-film as revealed by FE-SEM images and by SE analysis. Besides, with decreasing Ts, a slight increase of the LO/TO band intensity ratio is observed in Fig. 5c showing the normalized FTIR spectra in oblique incidence. This is due to the size decrease of the nanostructures as well as to the increase of their surfaces curvatures that both favor scattering and hence enhance the LO probe [13]. Besides, the larger variability of crystal orientations that are observed by XRD, would also enhance the LO/TO intensity ratio [31].

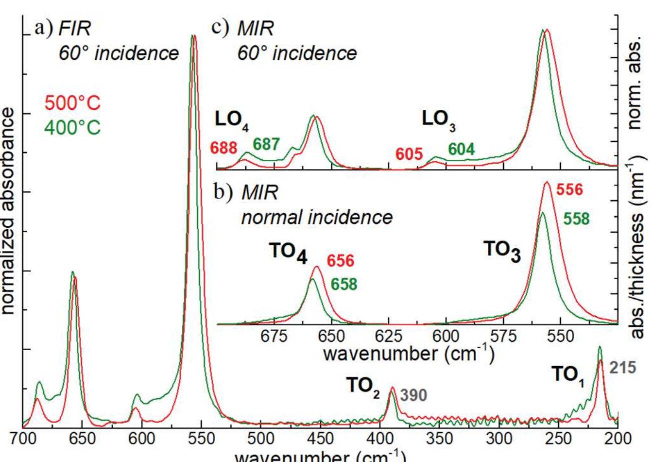

Fig. 5. 60° incidence angle normalized absorbance a) FIR-FTIR and b) MIR-FTIR spectra of Co_3O_4 thin films deposited on Si wafer at 400 °C and 500 °C. c) Normal incidence absorbance MIR-FTIR spectra divided by the thickness.

3.4. Electrical properties at macroscale

Fig. 6a shows the Arrhenius plot of the electrical resistivity ρ namely the variation of $\ln(\rho)$ with the inverse of the absolute temperature. The figure shows that the films are semiconducting and the non-linear nature of the plot shows that resistivity does not follow a simple activation energy mechanism. The room temperature electrical resistivities are 28.28 ± 0.04 and $87.54 \pm 0.05\,\Omega\,$cm, for Ts = 400 °C and 500 °C, respectively, which are close to literature results of crystalline Co_3O_4 thin films deposited by CVD [16], and by ALD [17,18]. On the other hand, our films show similar morphologies to those reported by ALD by Klepper et al. [18] but for smaller Ts ranging from 100 °C to 330 °C. The authors also observed a concomitant increase of the resistivity (0.5–10 Ω cm) with increasing the grains size (20–50 nm) while Ts was increased which would suggest that the conduction paths are along the grain boundaries and not through the grains. We further investigate the electrical properties of the films by AC Hall effect. The measurements demonstrate the p-type semiconductor behavior, and show that the increase of the resistivity is actually due to lower holes concentration as Ts is increased, while the mobility is not significantly impacted. The holes density are $N = 2.0 \pm 0.9 \times 10^{18}$ and $4.6 \pm 0.4 \times 10^{17}\,cm^{-3}$, and the mobilities are $\mu = 0.16$ and $0.11\,cm^2\,V^{-1}\,s^{-1}$ for Ts = 400 °C, and 500 °C, respectively. It has been earlier shown by Cheng et al. [16] that for carrier concentration in the range of $10^{18}\,cm^{-3}$, and for mobility values below $1\,cm^2\,V^{-1}\,s^{-1}$, the temperature dependence of the conductivity could be described by a VRH mechanism proposed by Mott [32]. The Mott VRH model of the temperature dependence of the resistivity is given by Refs. [33,34]: where σ_0 and T_0 are some Mott parameters, and n is an integer ranging from 1 to 4 that depends on the dimensionality, on the electronic-band structure near the Fermi level, and on the Coulomb correlations between electrons [34]. Since the latter equation can be written as:

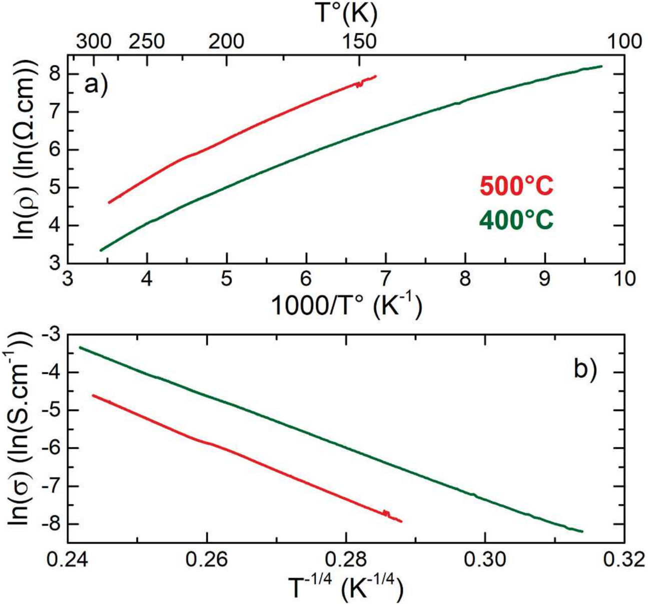

Fig. 6. a) Plot of ln(ρ) against (1000/T) and b) plot of ln(σ) against ($T^{-1/4}$) of Co_3O_4 thin films deposited on fused silica windows as a function of Ts.

$$\ln(\sigma) = \ln(\sigma_0) - \left(\frac{T_0}{T}\right)^{\frac{1}{n}},$$

we therefore have plotted the ln(ρ) vs the Mott VRH variable $T^{-1/n}$. The best linear relationship shown in Fig. 6b is obtained for n=4 suggesting a 3D VRH carrier transport mechanism of holes that occurs by energy transfer between Co^{3+} and Co^{2+} in the valence band [16].

3.5. Impact of the nanoscale morphology on the electrical properties

In order to localize the electric transport paths, we compare the surface morphology probed by AFM with the current measured in C-AFM mode at nanoscale. Fig. 7a and b highlight that the surface morphologies for layers deposited at 400 °C and 500 °C, respectively, are consistent with FE-SEM pictures shown in Fig. 2. Moreover, we found that the surface arithmetic roughness decreases from 13.1 to 9.9 nm with increasing Ts, which is in agreement with SE analysis, and consistent with the increase of the nanostructures size and density observed in FE-SEM. The current map of the films deposited at 400 °C is very inhomogeneous over the surface showing conduction areas exhibiting different conduction behavior (Fig. 7c). The lateral dimension of highly conductive areas is between 65 nm and 130 nm which correspond to the sizes of 1 or 2 nanostructures, respectively, in the topography map (Fig. 7a). In the current occurrence diagram shown in Fig. 7e, the current distribution can be distinguished in three conduction areas: *i)* a highly conductive area (labeled area-3) corresponding to 6% of the surface, *ii)* a low conductive area (area-2) which corresponds to 11% of the surface, and *iii)* the main area (area-1) of 83% of the surface which is non-conductive. The surface ratios are calculated by integration of the occurrence diagram. The current distribution over the surface (Fig. 7d) of the 500°C-film is more homogeneous and, one can see that the conduction areas are consistent with the parallelepiped nanostructures visible in Fig. 7b. However, some non-conductive areas are also present. They also indistinctly correspond to similar nanostructures. The current occurrence ratio diagram in Fig. 7f shows that the conductive area (area-2) represents 92.5% of the surface. The conductive areas show a linear behavior of the current versus the applied bias voltage (see Fig. 7g and h). As results, comparisons of the current map with the morphology of both the 400°C- and the 500°C-films suggest that the conduction paths are through the nanostructures and not along grain boundaries.

However, these local measurements emphasize that the depth average conduction over the surface is more important for the 500°C-film than for the 400°C-one, while the macroscale lateral measurements show (see section 3.4) that the resistivity is conversely higher for the 500°C-sample. Then, two hypotheses could be envisaged regarding the 400°C-film: *i)* Columnar nanostructures present different conductivities. According to C-AFM measurement around 80% of the nanostructures should be non-conductive. In this configuration, the lateral conduction which should occur nanostructures to nanostructures over a long conduction path is thus impossible because non conductive grains are too numerous. This hypothesis is then non-consistent with the macroscale lateral current measurements. *ii)* Columns could be highly conductive but the dense sublayer at the Si wafer interface presents high density of non-conductive grain (see Fig. 8a). In this configuration, the lateral surface conduction is then possible. The C-AFM current map would strongly depend on the conductivity of the dense layer at the substrate interface. The existence of the two conduction areas can be explained as follows: *i)* highly conductive areas corresponds to conductive columnar nanostructures in contact with conductive interface layer grains, *ii)* low conductive areas correspond to columnar nanostructures in contact or in the vicinity of the conductive interface layer grains. The conductivity can also strongly differ with the crystal direction of the nanocrystallites. The 500°C-film shows a higher texture that could result in a stronger direction dependence of the film conductivity. This could also explain the unexpected higher resistivity that shows the 500 °C film laterally to

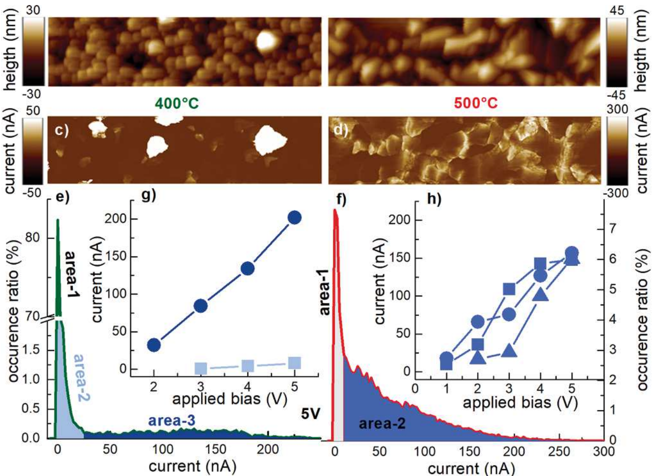

Fig. 7. a, b) AFM surface topography, and c, d) electric current map on the same area for 5 V-bias applied to the films deposited at 400 °C and 500 °C, respectively. Same x-scale of 2 μm is used for all maps. The current scales of c) is set to lower current values to optimize the contrast. e, f) Current occurrence diagram, and g, h) current versus applied voltage bias of the films deposited at 400 °C and 500 °C, respectively.

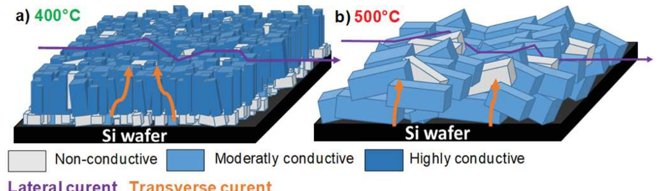

Fig. 8. Lateral and transverse conduction schematics of the films deposited at a) 400 °C and b) 500 °C on Si wafer.

the film surface (see Fig. 8b) compared to the 400°C-sample.

4. Conclusion

Polynanocrystalline Co_3O_4 films are deposited by pulsed liquid-gas injection thermal MOCVD, and the electrical properties of the films are studied for two different film morphologies resulting from two deposition temperatures. All films present a p-type semiconductor behavior with the best conduction properties obtained at 400 °C with a minimum room temperature film resistivity of 28.28 Ω cm, a maximum holes density of $2 \pm 0.8 \times 10^{18}$ cm^{-3}, and a maximum holes mobility of 0.16 cm^2 V^{-1} s^{-1}. Moreover, the linear $T^{-1/4}$ temperature dependence of the film conductivity is attributed to a 3D VRH carrier of holes. Nanoscale characterization emphasize that the conduction paths occurr through the Co_3O_4 grains.

Conflicts of interest

There are no conflicts of interest to declare.

Acknowledgments

This work was supported by a Toulouse Tech'Interlab. We are indebted to Diane Samelor, Daniel Sadowski, Cédric Charvillat, Olivier Marsan, Jérôme Esvan (CIRIMAT), Stéphane Leblond du Plouy, Sophie Gouy (UMS Castaing) for their contributions.

References

[1] H. Tüysüz, E.L. Salabaş, E. Bill, H. Bongard, B. Spliethoff, C.W. Lehmann, F. Schüth, Synthesis of hard magnetic ordered mesoporous $Co_3O_4/CoFe_2O_4$ nanocomposites, Chem. Mater. 24 (2012) 2493–2500, https://doi.org/10.1021/cm3005166.

[2] S.K. Meher, G.R. Rao, Ultralayered Co_3O_4 for high-performance supercapacitor applications, J. Phys. Chem. C 115 (2011) 15646–15654, https://doi.org/10.1021/jp201200e.

[3] A.A. Yadav, U.J. Chavan, Electrochemical supercapacitive performance of spray deposited Co3O4 thin film nanostructures, Electrochim. Acta 232 (2017) 370–376, https://doi.org/10.1016/j.electacta.2017.02.157.

[4] X.H. Xia, J.P. Tu, J. Zhang, J.Y. Xiang, X.L. Wang, X.B. Zhao, Fast electrochromic properties of self-supported Co_3O_4 nanowire array film, Sol. Energy Mater. Sol. Cells 94 (2010) 386–389, https://doi.org/10.1016/j.solmat.2009.08.020.

[5] M. Burriel, G. Garcia, J. Santiso, A.N. Hansson, S. Linderoth, A. Figueras, Co_3O_4 protective coatings prepared by pulsed injection metal organic chemical vapour deposition, Thin Solid Films 473 (2005) 98–103, https://doi.org/10.1016/j.tsf.2004.07.081.

[6] B. Kupfer, K. Majhi, D.A. Keller, Y. Bouhadana, S. Rühle, H.N. Barad, A. Y. Anderson, A. Zaban, Thin film Co3O4/TiO2 heterojunction solar cells, Adv. Energy Mater. 5 (2015) 2–6, https://doi.org/10.1002/aenm.201401007.

[7] J.W. Yoon, J.K. Choi, J.H. Lee, Design of a highly sensitive and selective C_2H_5OH sensor using p-type Co_3O_4 nanofibers, Sens. Actuators B Chem. 161 (2012) 570–577, https://doi.org/10.1016/j.snb.2011.11.002.

[8] W.Y. Li, L.N. Xu, J. Chen, Co_3O_4 nanomaterials in lithium-ion batteries and gas sensors, Adv. Funct. Mater. 15 (2005) 851–857, https://doi.org/10.1002/adfm.200400429.

[9] A. Gasparotto, D. Barreca, D. Bekermann, A. Devi, R. a Fischer, P. Fornasiero, V. Gombac, O.I. Lebedev, C. Maccato, T. Montini, G. Van Tendeloo, E. Tondello, F-Doped Co_3O_4 photocatalysts for sustainable H_2 generation from Water/Ethanol, J. Am. Chem. Soc. 133 (2011), https://doi.org/10.1021/ja210078d, 19362–5.

[10] K.J. Kormondy, A.B. Posadas, A. Slepko, A. Dhamdhere, D.J. Smith, K.N. Mitchell, T.I. Willett-Gies, S. Zollner, L.G. Marshall, J. Zhou, A.a. Demkov, Epitaxy of polar semiconductor Co3O4 (110): growth, structure, and characterization, J. Appl. Phys. 115 (2014) 1–9, https://doi.org/10.1063/1.4885048.

[11] L. Qiao, H.Y. Xiao, H.M. Meyer, J.N. Sun, C.M. Rouleau, A.A. Puretzky, D. B. Geohegan, I.N. Ivanov, M. Yoon, W.J. Weber, M.D. Biegalski, Nature of the band gap and origin of the electro-/photo-activity of Co3O4, J. Mater. Chem. C. 1 (2013) 4628, https://doi.org/10.1039/c3tc30861h.

[12] C.-M. Jiang, L. Robert Baker, J. Matthew Lucas, J. Vura-Weis, A. Paul Alivisatos, S. R. Leone, Characterization of Photo-Induced Charge Transfer and Hot Carrier Relaxation Pathways in Spinel Cobalt Oxide (Co_3O_4), (n.d.). doi:10.1021/jp5071133..

[13] Y. Li, W. Qiu, F. Qin, H. Fang, V.G. Hadjiev, D. Litvinov, J. Bao, Identification of cobalt oxides with Raman scattering and fourier transform infrared spectroscopy, J. Phys. Chem. C 120 (2016) 4511–4516, https://doi.org/10.1021/acs.jpcc.5b11185.

[14] E. Rios, G. Poillerat, J.F. Koenig, J.L. Gautier, P. Chartier, Preparation and characterization of thin Co3O4and MnCo2O4films prepared on glass/SnO2:F by spray pyrolysis at 150 °C for the oxygen electrode, Thin Solid Films 264 (1995) 18–24, https://doi.org/10.1016/0040-6090(95)06570-9.

[15] H. Tototzintle-Huitle, E. Prokhorov, A. Mendoza-Galván, J.E. Urbina, J. González-Hernández, Study of the formation of Co3O4 thin films using sol-gel method, J. Phys. Chem. Solids 64 (2003) 975–980, https://doi.org/10.1016/S0022-3697(02)00460-2.

[16] C.S. Cheng, M. Serizawa, H. Sakata, T. Hirayama, Electrical conductivity of Co3O4 films prepared by chemical vapour deposition, Mater. Chem. Phys. 53 (1998) 225–230, https://doi.org/10.1016/S0254-0584(98)00044-3.

[17] M.E. Donders, H.C.M. Knoops, M.C.M. van, W.M.M. Kessels, P.H.L. Notten, Remote plasma atomic layer deposition of Co3O4 thin films, J. Electrochem. Soc. 158 (2011) G92, https://doi.org/10.1149/1.3552616.

[18] K.B. Klepper, O. Nilsen, H. Fjellvåg, Growth of thin films of Co3O4 by atomic layer deposition, Thin Solid Films 515 (2007) 7772–7781, https://doi.org/10.1016/j.tsf.2007.03.182.

[19] M.E. Donders, H.C.M. Knoops, W.M.M. Kessels, P.H.L. Notten, Co3O4 as anode material for thin film micro-batteries prepared by remote plasma atomic layer deposition, J. Power Sources 203 (2012) 72–77, https://doi.org/10.1016/j.jpowsour.2011.12.020.

[20] V. Patil, P. Joshi, M. Chougule, S. Sen, Synthesis and characterization of Co 3 O 4 thin film, Soft Nanosci. Lett. 2 (2012) 1–7, https://doi.org/10.4236/snl.2012.21001.

[21] S.A. Makhlouf, Z.H. Bakr, K.I. Aly, M.S. Moustafa, Structural, electrical and optical properties of Co3O 4 nanoparticles, Superlattice Microstruct. 64 (2013) 107–117, https://doi.org/10.1016/j.spmi.2013.09.023.

[22] V.R. Shinde, S.B. Mahadik, T.P. Gujar, C.D. Lokhande, Supercapacitive cobalt oxide (Co_3O_4) thin films by spray pyrolysis, Appl. Surf. Sci. 252 (2006) 7487–7492, https://doi.org/10.1016/j.apsusc.2005.09.004.

[23] S.G. Victoria, A.M. Ezhil Raj, C. Ravidhas, An insight in the structural, morphological, electrical and optical properties of spray pyrolysed Co_3O_4 thin films, Mater. Chem. Phys. 162 (2015) 852–859, https://doi.org/10.1016/j.matchemphys.2015.07.015.

[24] P. Nkeng, J.-F. Koenig, J.L. Gautier, P. Chartier, G. Poillerat, Enhancement of surface areas of Co3O4 and NiCo2O4 electrocatalysts prepared by spray pyrolysis, J. Electroanal. Chem. 402 (1996) 81–89, https://doi.org/10.1016/0022-0728(95)04254-7.

[25] I.G. Aviziotis, N. Cheimarios, T. Duguet, C. Vahlas, A.G. Boudouvis, Multiscale modeling and experimental analysis of chemical vapor deposited aluminum films: linking reactor operating conditions with roughness evolution, Chem. Eng. Sci. 155 (2016) 449–458, https://doi.org/10.1016/J.CES.2016.08.039.

[26] H. Lee, C.H. Lee, I.S. Oh, I.M. Lee, A study on the development of CVD precursors VI-thermal properties of Co(III) β-diketonates, Bull. Korean Chem. Soc. 31 (2010) 891–894, https://doi.org/10.5012/bkcs.2010.31.04.891.

[27] Y. Chen, H.T. Yi, V. Podzorov, High-resolution ac measurements of the Hall effect in organic field-effect transistors, Phys. Rev. Appl. 5 (2016), https://doi.org/10.1103/PhysRevApplied.5.034008, 034008.

[28] M. Gunes, H. Sato, L. Pinsard-Gaudart, D. Berardan, N. Dragoe, A versatile system for Hall effect measurements at high temperature, Meas. Sci. Technol. 28 (2017) 105905, https://doi.org/10.1088/1361-6501/aa7fe1.

[29] T. Smart, T.A. Pham, Y. Ping, T. Ogitsu, The Nature of Band Gap of Co3O4 - a Revisit from First-Principles, APS March Meet. 2019, 2019. Abstr. Id.C11.006, http://adsabs.harvard.edu/abs/2019APS..MARC11006S. (Accessed 8 May 2019).

[30] D. Barreca, C. Massignan, S. Daolio, M. Fabrizio, C. Piccirillo, L. Armelao, E. Tondello, Composition and microstructure of cobalt oxide thin films obtained from a novel cobalt(II) precursor by chemical vapor deposition, Chem. Mater. 13 (2001) 588–593, https://doi.org/10.1021/cm001041x.

[31] C. Pecharromán, F. Gracía, J.P. Holgado, M. Ocaña, A.R. González-Elipe, J. Bassas, J. Santiso, A. Figueras, Determination of texture by infrared spectroscopy in titanium oxide–anatase thin films, J. Appl. Phys. 93 (2003) 4634–4645, https://doi.org/10.1063/1.1560858.

[32] N.F. Mott, Conduction in non-crystalline materials, Philos. Mag. 19 (1969) 835–852, https://doi.org/10.1080/14786436908216338.

[33] N.F. (Nevill F. Mott, E.A. (Edward A. Davis, Electronic Processes in Non-crystalline Materials, Oxford University Press, 2012, in: https://global.oup.com/academic/product/electronic-processes-in-non-crystalline-materials-9780199645336?cc=fr&lang=en&. (Accessed 15 May 2019).

[34] M. Shizuya, M. Isobe, Y. Baba, T. Nagai, M. Osada, K. Kosuda, S. Takenouchi, Y. Matsui, E. Takayama-Muromachi, New misfit-layered cobalt oxide (CaOH) 1.14CoO2, J. Solid State Chem. 180 (2007) 249–259, https://doi.org/10.1016/J.JSSC.2006.10.014.